



AFRL-RW-EG-TR-2016-092

Simulation of Flow for an Immersed Sphere

**Pedro A. Lopez-Fernandez
Ralph K. Tatum
Douglas V. Nance**

**Air Force Research Laboratory
Munitions Directorate/Ordnance Division
Lethality, Vulnerability and Survivability Branch
(AFRL/RWML)
Eglin AFB, FL 32542-5910**

December 2016

Interim Report

**Distribution A: Approved for public release; distribution unlimited.
Approval Confirmation 96TW-2016-0229 dated 12 December 2016**

**AIR FORCE RESEARCH LABORATORY
MUNITIONS DIRECTORATE**

NOTICE AND SIGNATURE PAGE

Using Government drawings, specifications, or other data included in this document for any purpose other than Government procurement does not in any obligate the U.S. Government. The fact that the Government formulated or supplied the drawings, specifications, or other data does not license the holder or any other person or corporation, or convey any rights or permission to manufacture, use, or sell any patented invention that may relate to them.

This report was cleared for public release by the 96th Air Base Wing, Public Affairs Office, and is available to the general public, including foreign nationals. Copies may be obtained from the Defense Technical Information Center (DTIC) < <http://www.dtic.mil/dtic/index/html>>.

AFRL-RW-EG-TR-2016-092 HAS BEEN REVIEWED AND IS APPROVED FOR PUBLICATION IN ACCORDANCE WITH ASSIGNED DISTRIBUTION STATEMENT.

FOR THE DIRECTOR:

//SIGNED//

HOWARD G. WHITE, PhD
Chief Engineer
Ordnance Division

//SIGNED//

KIRK J. VANDEN, PhD
Technical Advisor
Lethality, Vulnerability and Survivability Branch

//SIGNED//

PEDRO LOPEZ-FERNANDEZ
Program Manager
Lethality, Vulnerability and Survivability Branch

This report is published in the interest of scientific and technical information exchange, and its publication does not constitute the Government's approval or disapproval of its ideas or findings.

This page intentionally left blank

REPORT DOCUMENTATION PAGE				Form Approved OMB No. 0704-0188	
Public reporting burden for this collection of information is estimated to average 1 hour per response, including the time for reviewing instructions, searching existing data sources, gathering and maintaining the data needed, and completing and reviewing this collection of information. Send comments regarding this burden estimate or any other aspect of this collection of information, including suggestions for reducing this burden to Department of Defense, Washington Headquarters Services, Directorate for Information Operations and Reports (0704-0188), 1215 Jefferson Davis Highway, Suite 1204, Arlington, VA 22202-4302. Respondents should be aware that notwithstanding any other provision of law, no person shall be subject to any penalty for failing to comply with a collection of information if it does not display a currently valid OMB control number. PLEASE DO NOT RETURN YOUR FORM TO THE ABOVE ADDRESS.					
1. REPORT DATE (DD-MM-YYYY) 15-12-2016		2. REPORT TYPE Interim		3. DATES COVERED (From - To) 31-03-2016 – 31-07-2016	
4. TITLE AND SUBTITLE Simulation of Flow for an Immersed Sphere				5a. CONTRACT NUMBER	
				5b. GRANT NUMBER	
				5c. PROGRAM ELEMENT NUMBER 62602F	
6. AUTHOR(S) Pedro A. Lopez-Fernandez, Ralph K. Tatum, Douglas V. Nance				5d. PROJECT NUMBER 25024504	
				5e. TASK NUMBER	
				5f. WORK UNIT NUMBER W0TP	
7. PERFORMING ORGANIZATION NAME(S) AND ADDRESS(ES) Air Force Research Laboratory, Munitions Directorate Ordnance Division Lethality, Vulnerability, and Survivability Branch (AFRL/RWML) Eglin AFB FL 32542-6810				8. PERFORMING ORGANIZATION REPORT NUMBER AFRL-RW-EG-TR-2016-092	
9. SPONSORING / MONITORING AGENCY NAME(S) AND ADDRESS(ES) Air Force Research Laboratory, Munitions Directorate Ordnance Division Lethality, Vulnerability, and Survivability Branch (AFRL/RWML) Eglin AFB FL 32542-6810 Technical Advisor: Kirk J. Vanden, PhD				10. SPONSOR/MONITOR'S ACRONYM(S)	
				11. SPONSOR/MONITOR'S REPORT AFRL-RW-EG-TR-2016-092	
12. DISTRIBUTION / AVAILABILITY STATEMENT Distribution A: Approved for public release; distribution unlimited. Approval Confirmation 96W-2016-0229, dated 12 December 2016					
13. SUPPLEMENTARY NOTES					
14. ABSTRACT This report addresses a series of simulations of turbulent, multi-species flow fields surrounding a sphere. The purpose of these simulations is to validate our capability for using the Large Eddy Simulation with Linear Eddy Modeling in 3 Dimensions (LESLIE3D) multiphase physics computer program. A high Reynolds number flow field is computed at Mach 2.0, and a low Reynolds number flow field is calculated at Mach 0.1. The former flow field is strongly shocked while the latter flow field is shock wave free. In each test calculation, the physics of the flow field is examined, and the drag coefficients are calculated via post-processing for comparison with data. At the same time, drag post-processor algorithms are validated.					
15. SUBJECT TERMS CFD, Computational Fluid Dynamics, Sphere flow, LES, Large Eddy Simulation, LDKM, Locally Dynamic subgrid Kinetic energy Model MUSCL, Monotone Upstream centered Schemes for Conservation Laws, Navier-Stokes, LESLIE3D, Curved shock, Turbulent flow					
16. SECURITY CLASSIFICATION OF:			17. LIMITATION OF ABSTRACT	18. NUMBER OF PAGES	19a. NAME OF RESPONSIBLE PERSON
a. REPORT	b. ABSTRACT	c. THIS PAGE			Pedro A. Lopez-Fernandez
UNCLASSIFIED	UNCLASSIFIED	UNCLASSIFIED	SAR	41	19b. TELEPHONE NUMBER (include area code) 850-883-2707

This page intentionally left blank

Table of Contents

Section	Title	page
1.0	Summary	1
2.0	Introduction	2
3.0	Methods, Assumptions and Procedures	4
3.1	Navier-Stokes Equations	4
3.2	Filtered Navier-Stokes Equation for Large Eddy Simulation	6
3.3	LES Modeling Considerations for the Filtered Governing Equations	9
3.4	Numerical Algorithms	12
3.5	Problem Set-Up	18
4.0	Results	21
4.1	Supersonic Test Case – Flow Field Results	21
4.2	Subsonic Test Case – Flow Field Results	26
5.0	Conclusions	29
	References	30
	Acronyms	32

List of Figures

Figure	Title	Page
1.	Spherical grid with one block set aside for illustrative purposes.....	18
2.	Perturbation induced along an arc on the inner surface of block 10.....	18
3.	Grid block arrangement for the simulation of subsonic flow outside of the sphere	20
4.	Slice pressure plot on the xy -plane of the sphere flow field at Mach 2, units in Pascals.....	21
5.	Contoured slice pressure plot on the xy -plane of the sphere flow field at Mach 2, units in Pascals.....	21
6.	Full field slice temperature plot of the sphere flow field at Mach 2, units in Kelvin ..	22
7.	Contoured slice temperature plot of the sphere flow field at Mach 2, units in Kelvin.....	22
8.	Slice plot of u velocity with contours of velocity magnitude at 13.61 ms; units are m/s.....	22
9.	Slice plot of v velocity with contours of velocity magnitude at 13.61 ms; units are m/s.....	23
10.	Slice plot of w velocity with contours of velocity magnitude at 13.61 ms; units are m/s.....	23
11.	Time history plots for x -component of vorticity, units s^{-1}	23
12.	Time history plots for y -component of vorticity, units s^{-1}	24
13.	Time history plots for z -component of vorticity, units s^{-1}	24
14.	Time history plots for vorticity magnitude, units s^{-1}	25
15.	Time history plots for subgrid kinetic energy, units m^2/s^2	25
16.	Drag coefficient time history for the sphere at Mach 2.0	26
17.	Slice plot of the pressure field for the subsonic solution at 43.68 ms	27
18.	Slice plot of the temperature field for the subsonic solution at 43.68 ms.....	27
19.	Drag coefficient time history for the sphere at Mach 0.1	28

1.0 SUMMARY

This report addresses a series of simulations of turbulent, multi-species flow fields surrounding a sphere. The purpose of these simulations is to validate our capability for using the Large Eddy Simulation with Linear Eddy Modeling in 3 Dimensions (LESLIE3D) multiphase physics computer program. A high Reynolds number flow field is computed at Mach 2.0, and a low Reynolds number flow field is calculated at Mach 0.1. The former flow field is strongly shocked while the latter flow field is shock wave free. In each test calculation, the physics of the flow field is examined, and the drag coefficients are calculated via post-processing for comparison with data. At the same time, drag post-processor algorithms are validated.

2.0 INTRODUCTION

During the past three decades, research in the field of computational fluid dynamics (CFD) has shown remarkable progress. CFD computer codes are now widely applied in the commercial world for aircraft design with little requirement for wind tunnel testing. A wide range of flight conditions for subsonic, transonic, supersonic and hypersonic flight can now be addressed by continuum based CFD codes at nominal cost. The inclusion of more complex equations of state and finite rate chemical reaction algorithms allow the physics of propulsion systems to be solved such as the burning of fuel in gas turbine combustors. Intricate multiphase physics equations couple the behavior of gas phase CFD algorithms with dispersed fields of solid particles and/or liquid droplets. This innovation, associated with more recent efforts, allows the numerical analysis of the environment within burning solid rocket motors. Because of its influence on chemistry and on dispersed particle/droplet fields, turbulence becomes a dominant factor in the solution of engineering problems. Within the past decade, Large Eddy Simulation (LES) has evolved to become a major force in solving many types of multiphase problems. Modern LES advances beyond the older Reynolds Averaged Navier-Stokes (RANS) turbulence models by exploiting mathematical similarity between the resolved Leonard stress and the modeled subgrid stress. Through the use of proper closure terms, modern LES algorithms can now capture the correct rates for finite rate chemical reactions. All of these capabilities exist within LESLIE3D, the Large Eddy Simulation with LInear Eddy model in 3 Dimensions, a computer code developed by Professor Suresh Menon at the Georgia Institute of Technology.[1]

Guided by the technological needs of the Munitions Directorate, over the past fourteen years LESLIE3D has evolved from being designed for subsonic combustion applications to a versatile code suited for all flight regimes with dense multiphase fields. Its crowning achievement is found in its shock turbulence algorithms. In earlier days, shock capturing algorithms held a distinct conflict of interest with turbulence simulation algorithms. Shock capturing methods are overly dissipative tending to wash subtle turbulent fluctuations out of the numerical flow field. On the other hand, turbulence simulation schemes often apply centered difference stencils. Centered stencils do not respect the directionality of acoustic waves in the flow field causing destructive oscillations near shock waves. Careful research culminating in 2005 produced the hybrid scheme employed by LESLIE3D to combine a set of low dissipation shock capturing schemes with the highly accurate Locally Dynamic subgrid Kinetic energy Model (LDKM) developed by Professor Suresh Menon. These algorithms are core capabilities installed within the parallel, multi-block version of LESLIE3D applied for the problems discussed here.

An issue that routinely confronts computational physics computer codes is that of code validation. Without getting into details, validation is intended to ensure that the computer solution generated for a particular problem renders results that compare favorably either with experimental results or with archived or exact solutions. For the standpoint of the computational physicist, physics computer codes should be developed based on “unit experiments” that elucidate the core physics behind the problem in question. These experiments are highly controlled and above all, have repeatable results that form the foundation of a validation dataset. The impression of validation held by the project engineer (or the customer) is often different. The customer often views validation as involving the comparison of code results for a much larger, less well controlled test configuration. In many cases, the type of test performed is not truly repeatable. The statistical

variation for measured parameters may be much larger. As a result, comparisons between test and computer code results may differ to a greater degree. In many cases the differences result from unknown or imprecisely known aspects of the test. For example, the precise location of a solid wall or say, an accurate representation of the surface roughness of a wall may not be known. Secondly, the same parameter may change between different test realizations. Addressing this type of uncertainty goes beyond the basic computational physics equations. The field of uncertainty quantification (UQ) is required to address these issues. The interested reader is referred to [2] for a discussion of this field.

At first glance, validation certainly encompasses the performance of the computational physics computer code, but it also must address the post-processing algorithms used to transform code results into usable engineering parameters. As an example, many CFD codes produce files containing say, pressure, temperature and velocity components at each point in the flow field. These are critical physics properties of the flow field, but they are, in many cases, not directly useful to the engineer. Instead, the engineer requires knowledge of the force components (lift and drag) or aerodynamic moments. Also, it may be desirable to know the rotational character of the flow. In each case, the data provided by the computational physics computer program must be post-processed to extract the required data. This process involves algorithms that also require validation.

Our outstanding project needs involve the simulation of high speed, turbulent flow around solid bodies where flow separation may occur. It is important to compute forces on this type of configuration, so we have selected a sphere as the solid body, and our task is to compute the time varying forces exerted on it by the flow field. By comparing the average drag coefficient exhibited by the sphere against archival data, we obtain a validation point for the post-processing algorithms and for the user's LESLIE3D input. Documenting the results of this validation effort is the goal of this report.

3.0 METHODS, ASSUMPTIONS AND PROCEDURES

3.1 Navier-Stokes Equations

An assessment of the physics of high speed flow fields under normal atmospheric conditions (excluding free molecular flow in rarefied air) for common finite length scales implies the existence of high Reynolds number flow. In a simple interpretation, the Reynolds number, a dimensionless quantity, represents the ratio of inertial forces to viscous forces in the flow field.[3] The Reynolds number is defined as

$$\text{Re} = \frac{\rho V L}{\mu} \quad (1)$$

where ρ and V are the local flow density and speed. L is the characteristic length scale, and μ is the dynamic viscosity. Low Reynolds numbers are indicative of flows where viscous effects are dominant; turbulence is unlikely. In high Reynolds number flows, inertial effects are important and overwhelm viscous effects. These flow fields tend to incur instability that leads to the formation of turbulence. All real flow fields are governed by the conservation of mass, momentum, energy and chemical elements. In the continuum limit, these properties are conserved by the Navier-Stokes equations [4], i.e.,

$$\frac{\partial \rho}{\partial t} + \nabla \cdot (\rho \vec{V}) = 0 \quad (2)$$

is the conservation of mass (or continuity equation) where ρ is the density of the gas mixture and \vec{V} is the flow velocity vector. The time coordinate is t . The momentum equation may be written as

$$\frac{\partial(\rho \vec{V})}{\partial t} + \nabla \cdot (\rho \vec{V} \vec{V}) + \nabla P = \nabla \cdot \underline{\tau} \quad (3)$$

In equation (3), the construct $\vec{V} \vec{V}$ is the tensor (or dyad) product of the velocity vector with itself resulting in the second order advection tensor. The thermodynamic pressure is denoted by P . The final term in this equation is $\underline{\tau}$, the deviatoric stress tensor. It is in this term that the viscous effects are included. This tensor may be written in Cartesian components as

$$\underline{\tau} = \tau_{i,j} = \lambda \left(\frac{\partial u_k}{\partial x_k} \right) \delta_{i,j} + \mu \left(\frac{\partial u_i}{\partial x_j} + \frac{\partial u_j}{\partial x_i} \right) \quad (4)$$

where the velocity vector is denoted as $\vec{V} = (u_1, u_2, u_3)^T$. The parameter λ is denoted as the bulk viscosity coefficient. Using Stoke's hypothesis, this coefficient is usually expressed as

$$\lambda = - \left(\frac{2}{3} \right) \mu \quad (5)$$

Equation (3) is an expression of Newton's second law for the flow field in the absence of body forces. Note that equation (3) is vector valued. It actually represents three distinct scalar equations. The conservation of total energy is enforced by the energy equation, i.e.,

$$\frac{\partial(\rho E)}{\partial t} + \frac{\partial(\rho u_j E)}{\partial x_j} + \frac{\partial(u_j P)}{\partial x_j} = \frac{\partial(\tau_{i,j})}{\partial x_i} - \frac{\partial q_i}{\partial x_i} \quad (6)$$

where E is the total energy per unit mass given by

$$E = e + \frac{1}{2} u_i u_i \quad (7)$$

Note that the summation convention is in effect over repeated indices. Also, the internal energy per unit mass is denoted as

$$e_n = e_n^0 + \int_{T_0}^T C_{v,n}(\hat{T}) d\hat{T} \quad (8)$$

For a single calorically perfect gas, it is advantageous to use the form

$$e = C_v T \quad (9)$$

For species n , the constant volume specific heat is denoted $C_{v,n}$ while T is the absolute temperature. The final term in equation (6) represents the heat flux vector defined within the fluid; specifically,

$$q_i = -\kappa \frac{\partial T}{\partial x_i} + \rho \sum_{n=1}^N Y_n h_n V_{i,n} \quad (10)$$

where κ is the thermal conductivity of the fluid, and h_n is the sensible enthalpy of species n computed as

$$h_n = h_n^0 + \int_{T_0}^T C_{p,n}(\hat{T}) d\hat{T} \quad (11)$$

The system comprised of equations (2), (3) and (6) is the common system of conservative Navier-Stokes equation, but to achieve mathematical closure, the system must include an equation of state such as that for a perfect gas, i.e.,

$$P = \rho R T \quad (12)$$

R is the perfect gas constant; that is

$$R = \frac{R_{univ}}{MW} \quad (13)$$

In this case, R is written for a single species with molecular weight MW . For a mixture of N gaseous species, the perfect gas constant is written as

$$R_{mix} = R_{univ} \sum_{n=1}^N \frac{Y_n}{MW_n} \quad (14)$$

where Y_n is the mass fraction of the n^{th} species, and R_{univ} is the universal gas constant. The problems considered in this report involve more than one gaseous species. LESLIE3D has been

generalized to include multiple species, so the system of governing equations is augmented by a species equation that is written as

$$\frac{\partial(\rho Y_n)}{\partial t} + \frac{\partial}{\partial x_i} [\rho Y_n (u_i + V_{i,n})] = 0, \quad n = 1, \dots, N \quad (15)$$

where $V_{i,n}$ is the diffusion velocity defined by

$$V_{i,n} = - \left(\frac{D_n}{Y_n} \right) \frac{\partial Y_n}{\partial x_i} \quad (16)$$

D_n is the diffusion coefficient for species n . [5]

In equation (4), viscosity, a key property for viscous flow fields, is computed as

$$\mu = \mu_0 \left(\frac{T}{T_0} \right)^{3/2} \frac{T_0 + S}{T + S} \quad (17)$$

a relationship known as Sutherland's law where μ_0 and T_0 are the reference viscosity and temperature, respectively, and S is a constant. These parameters depend on the gaseous substance in question. To attain highly accurate results for mixtures of gases, a viscous transport model may be needed.

3.2 Filtered Navier-Stokes Equations for Large Eddy Simulation

Fundamentally, the Navier-Stokes equations are based upon the continuum hypothesis where it is assumed that mass is modeled as a mathematical continuum, not as a vast collection of tiny particles.[6] This assumption works quite well as long as the mean free path for molecular motion remains far smaller than the characteristic dimension of the immersed body. This assumption holds extremely well for the application described in this report. One may ask that, given the viability of these equations, why not solve them directly for the fluid properties of interest? Why resort to the added complexity of large eddy simulation? The answer to these questions is reliant on required grid resolution and its impact on computer memory. The reader may recall that the direct numerical solution of the Navier-Stokes equation is referred to as Direct Numerical Simulation (DNS). For DNS, if one knows the initial conditions well enough, the Navier-Stokes equations could, in theory, be solved to produce a highly accurate solution. The difficulty associated with this idea lies in grid resolution. Turbulence has a range of scales that must be resolved to grant an accurate solution.[7] Accordingly, the grid must be resolved well enough to capture the smallest scales. This grid resolution scale as the Reynolds number raised to the 9/4 power.[8] That is to say, a simulation where $Re = 8$ million requires a grid possessing about 3.4×10^{15} points. This figure still remains well beyond the capability of current computer designs. So DNS is confined to very small Reynolds numbers. Since DNS is not a viable option, we must exploit the separation between the scales of fluid and filter the Navier-Stokes equations in three-space. In doing so, we can separate the large scales of motion (for resolution via the governing equations) from the small scales of motion. Fluid activity at the smaller scales is modeled; thus, the large eddy simulation requires substantially less computational resources than does DNS. The mathematical development of the filtered equations is lengthy, so only the results are stated here.

For an in-depth discussion of the derivations, the interested reader is referred to [5].

The filtered mass conservation equation is written as

$$\frac{\partial \bar{\rho}}{\partial t} + \frac{\partial (\bar{\rho} \tilde{u}_i)}{\partial x_i} = 0 \quad (18)$$

where the overbar indicates the spatial (top hat, in this case) filter. The tilde notation indicates the use of mass (Favre) averaging, i.e.,

$$\tilde{u}_i = \frac{\overline{\rho u_i}}{\bar{\rho}} \quad (19)$$

The filtered momentum equation is derived by a similar process; this equation contains the modeled term $\tau_{i,j}^{sgs}$ and is written as

$$\frac{\partial (\bar{\rho} \tilde{u}_i)}{\partial t} + \frac{\partial}{\partial x_j} [\bar{\rho} \tilde{u}_i \tilde{u}_j + \bar{P} \delta_{i,j} + \tau_{i,j}^{sgs} - \overline{\tau_{ij}}] = 0 \quad (20)$$

More specifically, the subgrid stress tensor is given by

$$\tau_{i,j}^{sgs} = \bar{\rho} \left(\overbrace{u_i u_j}^{\sim} - \tilde{u}_i \tilde{u}_j \right) \quad (21)$$

Due to the presence of a correlation term, the subgrid stress (21) must be modeled. The filtered total energy equation may be written as

$$\frac{\partial (\bar{\rho} \tilde{E})}{\partial t} + \frac{\partial}{\partial x_j} [\bar{\rho} \tilde{u}_j \tilde{E} + \tilde{u}_j \bar{P} + \bar{q}_j - \tilde{u}_i \overline{\tau_{j,i}} + H_j^{sgs} + \sigma_j^{sgs}] = 0 \quad (22)$$

where

$$\bar{q}_j = -\kappa(\tilde{T}) \frac{\partial \tilde{T}}{\partial x_j} + \bar{\rho} \sum_{n=1}^N \tilde{Y}_n h_n(\tilde{T}) \tilde{V}_{i,n} + q_j^{sgs} \quad (23)$$

The modeled terms in this case are the subgrid total enthalpy flux, the subgrid viscous work and the subgrid heat flux q_j^{sgs} . [1] Respectively, these terms are mathematically defined as

$$H_i^{sgs} = \bar{\rho} \left[\overbrace{E u_i}^{\sim} - \tilde{E} \tilde{u}_i \right] + \left[\overline{P u_i} - \bar{P} \tilde{u}_i \right] \quad (24)$$

$$\sigma_i^{sgs} = \overbrace{u_j \tau_{j,i}}^{\sim} - \tilde{u}_j \bar{\tau}_{j,i} \quad (25)$$

The filtered total energy per unit mass is given by

$$\tilde{E} = \tilde{e} + \frac{1}{2} \tilde{u}_k \tilde{u}_k + k^{sgs} \quad (26)$$

where the subgrid kinetic energy is defined by

$$k^{sgs} = \frac{1}{2} \left[\overbrace{u_k u_k}^{\sim} - \tilde{u}_k \tilde{u}_k \right] \quad (27)$$

We can write the filtered species equation as shown below.

$$\frac{\partial(\bar{\rho} \tilde{Y}_n)}{\partial t} + \frac{\partial}{\partial x_i} \left[\bar{\rho} (\tilde{Y}_n \tilde{u}_i + \tilde{Y}_n \tilde{V}_{i,n}) + Y_{i,n}^{sgs} + \theta_{i,n}^{sgs} \right] = 0, \quad n = 1, \dots, N \quad (28)$$

The two subgrid closure terms existing in equation (26) are mathematically defined as

$$Y_{i,n}^{sgs} = \bar{\rho} \left[\overbrace{u_i Y_n}^{\sim} - \tilde{u}_i \tilde{Y}_n \right] \quad (29)$$

the subgrid convective species flux and

$$\theta_{i,n}^{sgs} = \bar{\rho} \left[\overbrace{V_{i,n} Y_n}^{\sim} - \tilde{V}_{i,n} \tilde{Y}_n \right] \quad (30)$$

the subgrid diffusive species flux.[1] As is the gas with the other governing equations, the multi-species perfect gas equation of state also requires filtering. The result is

$$\bar{P} = \bar{\rho} \left(\tilde{R} \tilde{T} + R_{univ} T^{sgs} \right) \quad (31)$$

This equation of state contains T^{sgs} , the temperature-species correlation given mathematically as

$$T^{sgs} = \sum_{n=1}^N \left[\frac{\widetilde{\widetilde{Y_n T}} - \widetilde{Y_n} \widetilde{T}}{MW_n} \right] \quad (32)$$

The internal energy must also be filtered. It can be shown for calorically perfect gases that

$$\tilde{e} = \sum_{n=1}^N \left(C_{v,n} \widetilde{Y_n} \widetilde{T} + \widetilde{Y_n} \Delta h'_{f,n} \right) \quad (33)$$

where $\Delta h'_{f,n}$ is the standard heat of formation at T^0 , a reference temperature. Specifically,

$$\Delta h'_{f,n} = \Delta h_{f,n}^0 - C_{p,n} T^0 \quad (34)$$

3.3 LES Modeling Considerations for the Filtered Governing Equations

A significant investment in research time has been made to adapt the LES framework briefly discussed above for fully compressible flow fields. As it happens, a key aspect involved in formulating a compressible model entails altering the evolution equation for the subgrid kinetic energy. Although this equation acts, in some sense, like a governing equation, it is, in effect, a model, so it presented in this section of the report. An earlier form [9] of the subgrid kinetic energy equation is written as

$$\frac{\partial \bar{\rho} k^{sgs}}{\partial t} + \frac{\partial}{\partial x_i} (\bar{\rho} \tilde{u}_i k^{sgs}) = P^{sgs} - \varepsilon^{sgs} + \frac{\partial}{\partial x_i} \left(\bar{\rho} \frac{\nu_t}{Pr_t} \frac{\partial k^{sgs}}{\partial x_i} \right) \quad (35)$$

where the production and dissipation terms are, as one may suspect, modeled as

$$P^{sgs} = - \tau_{i,j}^{sgs} \frac{\partial \tilde{u}_i}{\partial x_j} \quad (36)$$

$$\varepsilon = C_\varepsilon \frac{k_{sgs}^{3/2}}{\Delta} \quad (37)$$

The parameter ν_t is the turbulent eddy viscosity, and Pr_t is the turbulent Prandtl number. The width of the filter is given by Δ , and C_ε is a parameter that is automatically adjustable.

As one may suspect, each term in this equation has a specific meaning. The first and second terms on the left side of the equation are the local and convective rates, respectively. On the right side of the equation, we have the production, dissipation and diffusion terms, respectively, for subgrid kinetic energy. Equation (33) is suited moreover for lower speed flows where compressibility effects are small. Modifications are required for the inclusion of major compressibility. A modified form that does include Mach number effects may be written as

$$\frac{\partial}{\partial t} \bar{\rho} k^{sgs} + \frac{\partial}{\partial x_i} (\bar{\rho} \tilde{u}_i k^{sgs}) = T_{k^{sgs}} + \wp_{k^{sgs}} + P_{k^{sgs}} - D_{k^{sgs}} \quad (38)$$

The terms on the right side of (36) are the diffusion, pressure-dilatation correlation, production and dissipation, respectively, for subgrid kinetic energy. The diffusion, pressure-dilatation correlation and dissipation cannot be directly computed from resolved scale quantities, so these terms require modeling based, in part, upon their mathematical definitions. In the interest of brevity, only the final subgrid kinetic energy equation is presented here.[5]

$$\begin{aligned} \frac{\partial}{\partial t} \bar{\rho} k^{sgs} + \frac{\partial}{\partial x_i} (\bar{\rho} \tilde{u}_i k^{sgs}) = & \frac{\partial}{\partial x_i} \left[(\bar{\rho} v_t + \mu) \frac{\partial k^{sgs}}{\partial x_i} + \frac{\bar{\rho} v_t \tilde{R}}{Pr_t} \frac{\partial \tilde{T}}{\partial x_i} \right] \\ & - \left[1 + \alpha_{\wp} (M_t^{sgs})^2 \left(\frac{\bar{\rho} \tilde{S} k^{sgs}}{D_{k^{sgs}}} \right)^2 \right] \left[\tau_{i,j}^{sgs} \frac{\partial \tilde{u}_j}{\partial x_i} + \bar{\rho} C_{\varepsilon} \frac{(k^{sgs})^{3/2}}{\Delta} \right] \end{aligned} \quad (39)$$

where v_t is the turbulent eddy viscosity; μ is the dynamic viscosity, and \tilde{R} is the mass-averaged mixture perfect gas constant. M_t^{sgs} is the turbulent Mach number based upon k^{sgs} . Also, we have that

$$\tilde{S} = \sqrt{\frac{1}{2} (\tilde{S}_{i,j} \tilde{S}_{i,j})} \quad (40)$$

where

$$S_{i,j} = \frac{1}{2} \left(\frac{\partial u_i}{\partial x_j} + \frac{\partial u_j}{\partial x_i} \right) \quad (41)$$

A major difference existing in the new subgrid kinetic energy equation (38) is that the pressure-dilatation correlation, as shown as the second line in the equation, is expressed as a Mach number dependent quantity; the parameter α_{\wp} is a model coefficient. A new expression for the dissipation of turbulent subgrid kinetic energy, $D_{k^{sgs}}$, is utilized, i.e.,

$$D_{k^{sgs}} = \frac{\bar{\rho} C_{\varepsilon} (k^{sgs})^{3/2}}{\Delta} \quad (42)$$

As described above, the subgrid kinetic energy is an important property in modeling turbulence in the flow field. Directly dependent upon this property is the subgrid stress tensor. It is modeled as follows.

$$\tau_{i,j}^{sgs} = -2\bar{\rho} v_t \left(\tilde{S}_{i,j} - \frac{1}{3} \tilde{S}_{k,k} \delta_{i,j} \right) + \frac{2}{3} k^{sgs} \delta_{i,j} \quad (43)$$

With subgrid kinetic energy provided by the solution to (38), (42) becomes mathematically closed. Basic model coefficients may be obtained for the turbulent eddy viscosity and dissipation. Note that

$$\nu_t = C_\nu \sqrt{k^{sgs}} \Delta \quad (44)$$

and

$$\varepsilon = C_\varepsilon \frac{(k^{sgs})^{3/2}}{\Delta} \quad (45)$$

An examination of turbulent spectra [10] shows that good values for C_ν and C_ε can be estimated as

$$C_\nu = 0.067 ; C_\varepsilon = 0.916 \quad (46)$$

Other values are possible for these coefficients, and dynamic evaluation of these coefficients is a validated option in LESLIE3D. Since this variant is not applied in the present work, it is not discussed here.

There are other modeling terms that arise from the filtering process. A brief discussion of these terms is warranted. Recall the filtered total energy equation (21). The closure terms that arise in this equation are the subgrid total enthalpy flux H_i^{sgs} (22) and the subgrid viscous work σ_i^{sgs} (23); accordingly, they are modeled [5] as a sum, i.e.,

$$H_i^{sgs} + \sigma_i^{sgs} = -(\bar{\rho}\nu_t + \mu) \frac{\partial k^{sgs}}{\partial x_i} - \frac{\bar{\rho}\nu_t C_P}{Pr_t} \frac{\partial \tilde{T}}{\partial x_i} + \tilde{u}_j \tau_{i,j}^{sgs} \quad (47)$$

All of the terms on the right side of (45) are either already modeled, known parameters or properties extracted from the resolved field. The first two terms on the right side are developed by a process known as gradient modeling since each involves a gradient computed from another flow property. A similar form exists for the subgrid convective species flux $Y_{i,n}^{sgs}$ in (28). That is

$$Y_{i,n}^{sgs} = -\left(\frac{\bar{\rho}\nu_t}{Sc_t}\right) \frac{\partial \tilde{Y}_n}{\partial x_i} \quad (48)$$

In the above equations, one notes the presence of the turbulent Schmidt number Sc_t , the ratio of the turbulent viscous diffusion rate to the molecular diffusion rate. This dimensionless number is taken as unity.[1] The subgrid species diffusive flux term $\theta_{i,n}^{sgs}$ in (29) is regarded as small in high Reynolds number flow fields, so it is neglected. The temperature-species correlation term T^{sgs} (30) is also believed to be very small in magnitude, so it too is neglected as is the subgrid heat flux q_j^{sgs} introduced in (22).

The equations shown in Section 2 represent a translation of physical laws (conservation equations, equation of state) into the language of mathematics. This process serves to formulate a mathematical model for fluid flow, but it is not without assumptions. This system of equations is built upon the continuum hypothesis, and although it is somewhat tacit, a Cartesian coordinate system resides under the mathematics. It is also worth mentioning that the perfect gas equation of state is, in fact, a model, an interpretation of reality not entirely unlike a drawing made by an illustrator. Regarding the scenarios for which they are designed, these equations are sound and

form a reliable and quantifiable mathematical model. Still, one should never lose sight of the fact that this system of equations is only a sketch of reality, albeit a detailed one. In Section 3, we learn that it is not currently possible for us to extract the level of detail inherent in this mathematical model. A primary inhibitor is the lack of computer memory. A more surreptitious difficulty is that at the same scales, we may be unable to accurately describe both boundary and initial conditions. For this reason, we back away from the fine scale and take a more macroscale view of the problem. That is to say, we apply filters to the mathematical flow field and extract “averaged” or “filtered” flow field properties in space. This process lacks neatness in that it introduces closure terms that must be modeled via a set of auxiliary equations that sit aside from the conservation laws requiring, in some cases, the use of empirical data and curve fitting. In the mathematical sense, closure terms add variables to the system. For that reason, we must add equations to the system to affect closure and admit a solution. Section 4 introduces specific closure term models including the time and space dependent model for subgrid kinetic energy, a property used to elucidate the subgrid stress tensor. In fact, subgrid kinetic energy is governed by an evolution equation. It is interesting to realize that although this equation has a production term, it is not capable of predicting the development of turbulence where none exists as an initial value. This equation is “sourceless”. One must prescribe a turbulent field, one with non-zero subgrid kinetic energy and non-zero velocity components, *a priori*. A non-turbulent flow field simply evolves with zero turbulence. Then one may ask, of what good is the subgrid kinetic energy equation if it cannot predict the creation of turbulence? The answer to this question is provided through an understanding of the evolution equation. The evolution equation describes how a property evolves from a presumed initial value. Suppose that a non-physically weak field of turbulence is prescribed at the initial condition. If so, the evolution equation alters this field based upon other physical inputs and strengthens the turbulent field. On the other hand, suppose that a turbulent field is prescribed where little or no turbulence really exists. In this case, based upon other physical inputs, in time the evolution equation depletes away the turbulent field as though none ever existed; the dissipation term dominates the equation. The subgrid kinetic energy equation endeavors to ensure that the evolving turbulent field is physically realizable.

3.4 Numerical Algorithms

In the preceding three sections of this report, we introduced and discussed the Navier-Stokes equations for multi-species, non-reacting flow fields. Then spatial filtering is applied to the equations, and the resulting closure terms are modeled. This development is largely mathematical; we have not discussed any of the numerical methods associated with solving these equations. In this section of the report, we present a brief discussion of the core solver methodology; the details are omitted because a full description of LESLIE3D’s numerical algorithms is very lengthy and covers many years of research. For these details, the interested reader is referred to References [5] and [10].

It is worthwhile to sketch the basic layout of LESLIE3D. The version used to support the present work is referred to as the “SVN code”, a loose designation named for the source code control method used for its development. The SVN code is admittedly an older computer code that is used predominantly for research, and it contains the primary computational physics algorithms for solving a wide array of problems. A principal capability of LESLIE3D is that it is a multi-block computer program. The computational domain is broken apart into “blocks” of grid. As a result,

LESLIE3D can solve problems on irregular geometries such as winged bodies like aircraft, or on the spherical shell used for problems addressed later in this report. Through the Message Passing Interface (MPI), the data associated with these blocks can communicate with more blocks being assigned to a processor or core. It follows that LESLIE3D is also fully parallelized. It ports and operates in parallel to a wide variety of computer systems including LINUX and CRAY clusters. Problems of local interest have been run on over 4,000 cores.

A structured grid must be generated for each block. For three-dimensional problems, this requirement implies that there is a local (i, j, k) index system assigned to the block, so each grid point has its own ordered index triplet (i, j, k) . One can “navigate” through the grid in simple counting order where

$$i = 1, 2, \dots, \text{IMAX}; \quad j = 1, 2, \dots, \text{JMAX}, \text{ and } k = 1, 2, \dots, \text{KMAX}.$$

The index maxima IMAX, JMAX and KMAX can, with some restrictions, differ for each block. Moreover, it follows that each block has six sides forming a hexahedron in the computational plane. Specifically, a given block has a side where $i = 1$ and a side where $i = \text{IMAX}$. The other sides of the block correspond to indices j and k . It is on each of these block sides (or interfaces) that either boundary conditions are enforced and/or parallel communication is established. A restriction on maximum block indices arises at the block sides. LESLIE3D presumes that block grids are constructed point-on-point. This statement implies that if two blocks communicate on a particular interface, then both blocks possess the same points on the interface. As a result, both blocks must share the same maximum lateral indices along the side shared by the blocks. That having been written, the “direction” of say, index i in one block need not be the same as an adjoining block. This property also applies to the other indices. Another restriction is that the index systems in each block must be right-handed in the physical space.

One may correctly surmise that LESLIE3D is a structured finite volume code. The hexahedral topology of a computational block extends to its interior, so the block is comprised of hexahedral cells. Since the grid is structured, if a block has maximum grid indices IMAX, JMAX and KMAX, then the cell indices will have maxima IMAX-1, JMAX-1 and KMAX-1. It follows that the total number of cells for the block is $(\text{IMAX}-1) \times (\text{JMAX}-1) \times (\text{KMAX}-1)$. Neither the blocks nor the finite volumes need to be brick-shaped. LESLIE3D easily allows arbitrary geometries; a Cartesian grid system is not required. LESLIE3D computes cell normal vectors and metrics as required for both the advective and viscous terms. A general curvilinear coordinate transformation is inherent in the coding. A strength of the finite volume method is noted when examining the governing equations. Although significant manipulation is required to achieve it, the system of governing equations can be written in the vector form

$$\frac{\partial \vec{Q}}{\partial t} + \nabla \cdot \vec{F} = 0 \quad (49)$$

In this expression, \vec{Q} is the vector of conserved variables i.e.,

$$\vec{Q} = \{\rho, \rho u, \rho v, \rho w, \rho E, \rho k^{sgs}, \rho Y_1, \dots, \rho Y_N\}^T \quad (50)$$

The construct $\vec{\vec{F}}$ is a vector of flux vectors containing all of the advective and viscous terms found in the governing equations. It may be expressed as

$$\vec{\vec{F}} = [\hat{i}\vec{F}_x, \hat{j}\vec{F}_y, \hat{k}\vec{F}_z] \quad (51)$$

where \hat{i} , \hat{j} and \hat{k} are the Cartesian unit vectors. On the other hand, vectors such as \vec{Q} , \vec{F}_x , \vec{F}_y and \vec{F}_z are not geometric vectors in three-space (\mathfrak{R}^3); rather, they are vectors in the sense that they are linear arrays of length $6+N$. To see the contents of the vectors in (51), consult reference [5]. To achieve a versatile numerical form for (47), we integrate this equation over a finite volume cell of volume V .

$$\iiint_V \frac{\partial \vec{Q}}{\partial t} dV + \iiint_V \nabla \cdot \vec{\vec{F}} dV = 0 \quad (52)$$

We note that the first integral is time independent, so for this term, the order of differentiation and integration may be interchanged. To the second integral, the divergence theorem is applied; hence,

$$\frac{\partial}{\partial t} \iiint_V \vec{Q} + \oint_{\partial(V)} \vec{\vec{F}} \cdot d\vec{S} = 0 \quad (53)$$

An interesting fact concerning (53) is that the second integral has been reduced to an integral over the closed surface (denoted $\partial(V)$) surrounding the finite volume cell. The leftmost integral in (53) contains the volume integral of the vector of conserved variables. This integral can be envisioned as the volume average of \vec{Q} multiplied by the cell volume. With this assertion in mind, let us evaluate (53) for cell (i, j, k) . We obtain

$$V_{i,j,k} \frac{d\vec{Q}_{i,j,k}}{dt} = - \oint_{\partial(V_{i,j,k})} \vec{\vec{F}} \cdot d\vec{S} \quad (54)$$

or

$$\frac{d\vec{Q}_{i,j,k}}{dt} = - \left(\frac{1}{V_{i,j,k}} \right) \oint_{\partial(V_{i,j,k})} \vec{\vec{F}} \cdot d\vec{S} \quad (55)$$

This procedure has reduced the system of governing equations to a system of ordinary differential equations, one for each cell. Recalling that the finite volume cells are six-sided (hexahedral), the surface integral is performed over six planar sides indexed by s . By implementing this idea, we have that

$$\frac{d\vec{Q}_{i,j,k}}{dt} = - \left(\frac{1}{V_{i,j,k}} \right) \sum_{s=1}^6 \vec{F}_{i,j,k}^s \cdot \hat{n}_s \Delta s \quad (56)$$

where \hat{n}_s is the outward pointing normal vector for cell side s , and Δs is the area of the side. The construct $\vec{F}_{i,j,k}^s$ is the flux vector evaluated at side s of cell (i, j, k) . Equation (56) is in what is referred to a semi-discrete form. The right side of this equation is discretized pending the

mechanics of the space scheme while the left side is an ordinary time derivative. Of course, the $V_{i,j,k}$ are the cell volumes. The left side still remains to be discretized.

To accurately resolve wave motion in a given flow field, LESLIE3D is developed with an “explicit” time marching algorithm. That is to say, the solution at time step $N+1$ relies only upon the solution computed at time N . This property of the solver renders highly accurate numerical solutions for waves with minimal numerical dissipation, and it streamlines the structure of the code. A disadvantage is that often a very small time step size is required to maintain stability for the numerical solution. Of course, LESLIE3D adjusts its time step automatically. The time marching scheme involved is a relatively simple Runge-Kutta method devised for integrating ordinary differential equations.[12] If we regard the right side of (54) as $\Delta Q / \Delta t$, then this scheme may be written in two steps as

$$\begin{aligned}\overline{Q^a} &= \overline{Q^n} + \Delta \overline{Q^n} \\ \overline{Q^{n+1}} &= \frac{1}{2} [\overline{Q^n} + \overline{Q^a} + \Delta \overline{Q^a}]\end{aligned}\tag{57}$$

In this case, $\overline{Q^a}$ is the intermediate solution between times n and $n+1$. Given the small time steps required for stability, this time stepping scheme is very accurate.

The larger portion of the work associated with the computation of a LESLIE3D solution lies in accomplishing the integration in space, i.e., calculating the sum in equation (56). Years ago, LESLIE3D was really developed with the use of second and fourth order MacCormack schemes.[5] For shock free flow fields, these schemes work quite well. Possessing very little dissipation, these space schemes capture turbulent motions in the flow field with great accuracy. Unfortunately, when LESLIE3D was adapted for shocked flowfields, the MacCormack scheme performed poorly (as expected). MacCormack methods are basically centered finite difference schemes meaning that information on the grid is weighted symmetrically in all directions. Shocked flow fields contain shock waves, and in the vicinity of a shock wave information does not arrive from all directions. Rather, the flow of information has a preferential direction. In fact, it comes from upstream of the shock wave, and the numerical algorithms to capture shock waves must be written accordingly. The associated algorithms are called upwind algorithms for this reason. There are many upwind algorithms divided into two major subdivisions: flux vector splitting schemes and flux difference splitting schemes. Generally, for problems that involve more complicated equations of state, flux difference splitting methods are preferred. These schemes are closely related to Godunov's method, but where Godonov's scheme entails an exact solution for the Riemann problem, flux difference splitting schemes tend to use approximate Riemann solvers.[13,14] The Riemann problem basically addresses the flow solution that occurs at a discontinuity. A discontinuity can be thought of as two volumes of gas separated by a fictitious, massless barrier that vanishes at the start of the problem. On one side of the barrier, we may have high pressure, temperature and density while on the other side, these properties have lower magnitudes. We apply this idea at every cell side in the flow field. Approximate Riemann solvers, like Roe's solver [15], provide an *exact solution* for this problem at each interface. Roe's method is of substantial theoretical interest, but it difficult to apply for complicated equations of state.[16] Other methods that do not so heavily rely on a mechanical characteristic wave decomposition are

preferred for general application.

This effort has encountered great success with variations of the Harten, Lax and van Leer (HLL) family of schemes. Departing from the strict flux difference splitting form for the flux, i.e.,

$$d\vec{F} = A d\vec{Q} \quad (58)$$

where A is a flux Jacobian matrix, the Riemann problem is sketched as an entity in space-time coordinate system. Space, in this regard, is cast in one dimension. For a simple description of the HLL solver, suppose a discontinuity is initiated at $x = 0$; the solution is formulated by one left traveling wave and one right traveling wave.[17] The x direction, as it were, is aligned perpendicular to the discontinuity (or interface). The HLL method is built upon an integral form of the Euler equations. Note that the Euler equations are considered in this analysis because upwind methods are designed for advective terms. The Navier-Stokes equations possess the same advective terms. The integral form is obtained as follows. The vector form (51) of our system of conservation laws can be written aligned perpendicular to an interface as

$$\frac{\partial \vec{Q}}{\partial t} - \frac{\partial \vec{F}}{\partial x} = 0 \quad (59)$$

By performing a cyclical integral around the rectangular x - t region, we have that

$$\oint \left(\frac{\partial \vec{Q}}{\partial t} - \frac{\partial \vec{F}}{\partial x} \right) dx dt = 0 \quad (60)$$

Hence,

$$\oint (\vec{Q} dx - \vec{F} dt) = 0 \quad (61)$$

The multi-component, non-geometric, vectors \vec{Q} and \vec{F} are easily evaluated on the fixed x and fixed t rectangular boundaries of this region resulting in a system of equations that relate their components allowing the shock properties to be calculated. To the left of the left traveling wave, the properties are uniform with values \vec{Q}_L with a uniform flux vector \vec{F}_L . The wave is assumed to propagate with speed S_L . Corresponding values for the right traveling wave are \vec{Q}_R , \vec{F}_R and S_R , respectively. The region in between the left and right traveling waves is assumed to have the uniform properties \vec{Q}^* and flux \vec{F}^* . Equation (61) can then be evaluated on the perimeter of the rectangular x - t region to show that

$$\vec{Q}^* = \frac{\vec{F}_L - S_L \vec{Q}_L - (F^R - S^R \vec{Q}^R)}{S_R - S_L} \quad (62)$$

as the properties vector in the region between the waves. After applying (61) across the individual left and right waves, it can be shown that

$$\vec{F}^* = \frac{S^R \vec{F}_L - S_L \vec{F}^R - S_L S_R (\vec{Q}_R - \vec{Q}_L)}{S_R - S_L} \quad (63)$$

is the flux vector for the region between the waves. The upwind flux is then defined at the interface (located here at $x = 0$, but at the cell side in practice) as

$$\vec{F}^{HLL} = \begin{cases} \vec{F}_L & 0 \leq S_L \\ \vec{F}^* & S_L \leq 0 \leq S_R \\ \vec{F}_R & S_R \leq 0 \end{cases} \quad (64)$$

The left and right wave speeds must still be estimated before this method is utilized. Commonly used wave speed estimates are provided by the work of Einfeldt.[18] These estimates are

$$S_L = \min[V_L - c_L, \langle V \rangle - \langle c \rangle] \quad (65)$$

$$S_R = \max[V_R + c_R, \langle V \rangle + \langle c \rangle] \quad (66)$$

The angle brackets used in (65) and (66) are indicative of the use of a Roe average. The HLL method is not difficult to implement, but it does have one disadvantage. It does not recognize the presence of a contact discontinuity between the waves. Instead the solution is effectively smeared across this region. The contact discontinuity is added back into the Riemann problem solution in the HLLC solver.[19] Due to the additional complexity of this solver and in keeping with the brevity of this report, HLLC is not derived here.

There are many important aspects of upwind solvers that cannot be included in this brief report. Among these are interface variable reconstruction schemes, total variation diminishing (TVD) schemes (limiters) and others that allow first order upwind scheme solutions like HLL to be extrapolated to higher order. For those readers who are interested, refer to References [5], [11] and [13]; many other such references also exist in the public domain.

Another core capability of LESLIE3D's algorithms that requires mention is the hybrid shock-turbulence capture scheme. Earlier in the report, it is mentioned that the algorithms for capturing shocks clash with the algorithms for capturing turbulence in the flow field. The former adds a significant amount of numerical viscosity while the latter abhors it. LESLIE3D possesses a specially modified HLLC shock-capturing scheme that includes some of the features of the Piecewise Parabolic Method (PPM) [20] to create an approximate Riemann solver that has very little excess numerical dissipation. Secondly, LESLIE3D adapts a special switching method to only apply the pure upwind solver in regions where discontinuities are detected. In smooth regions of flow, the MacCormack scheme is employed to accurately capture turbulence. The upwind method is adjoined carefully to the MacCormack scheme through a special shock detection algorithm to ensure that the appropriate solver algorithm is turned on at the appropriate time.

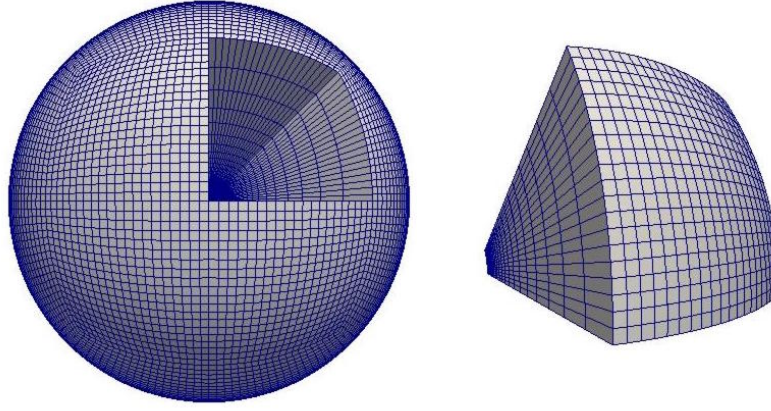


Figure 1. Spherical grid with one block set aside for illustrative purposes

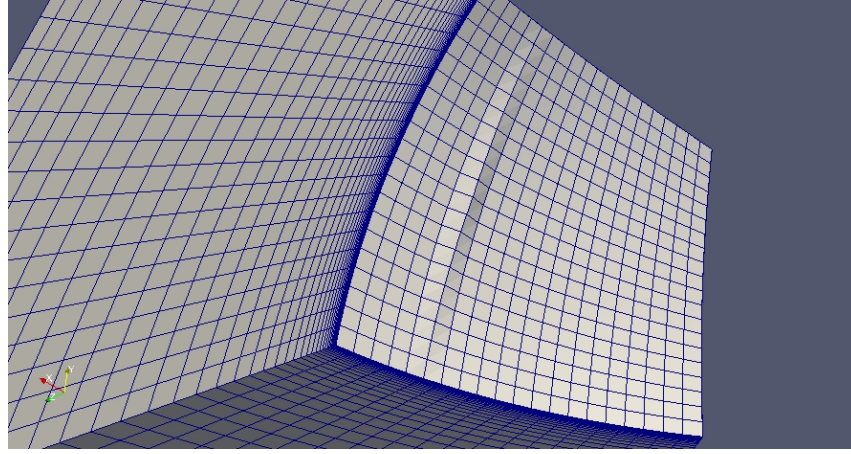


Figure 2. Perturbation induced along an arc on the inner surface of block 10

3.5 Problem Set-Up

As mentioned near the beginning of this report, the problem at hand is to validate post-processing computer codes developed in-house against physical parameters for a known flow configuration. Due to the substantial amount of available drag data, flow around a sphere is selected for study, and the key parameter for comparison is the average drag coefficient. In truth, we expect that the drag coefficient is somewhat time dependent, perhaps with some periodic character depending on the Reynolds number. Naturally, a grid must be generated for this configuration. The general form of a spherical shell is chosen. The flow field grid exists between the inner and outer spherical surfaces. Figure 1 illustrates this concept. The grid is produced by rotating key vectors one onto another with the origin as a vertex. In particular, an octant is divided into three grid volumes by selecting a central vector for the octant. For example, the first octant is delineated by the vectors:

$$\vec{V}_1 = (1,0,0); \quad \vec{V}_2 = (0,1,0); \quad \vec{V}_3 = (0,0,1) \quad (67)$$

This volume can be divided into three smaller volumes of equal size and shape by adding the

vector

$$\vec{V}_c = \left(\frac{1}{\sqrt{3}}, \frac{1}{\sqrt{3}}, \frac{1}{\sqrt{3}} \right) \quad (68)$$

as the central vector. Accomplishing this procedure in each of the eight octants between the inner and outer spherical shells leads to the formation of 24 volumes or blocks. To facilitate viscous spacing, the grid is stretched in the radial direction equivalently in each block. A simple finite geometric series is used as the stretching function. The spherical shell grid has inner and outer radii of 0.1 meter and 1 meter, respectively. For this test case, the minimum spacing at the sphere's surface is set at 10^{-4} meter. To provide for LESLIE3D's multi-block data communication, two ghost surfaces are installed adjacent to each of the six boundary surfaces for each block. For those surfaces that communicate to an adjacent block, the ghost surfaces must precisely overlay on the adjacent block's grid surfaces. If there is a mismatch in the ghost point locations, errors quickly arise in LESLIE3D's derivative computations. A final issue that sometimes arises for this type of problem is that of flow symmetry. The geometry of this grid configuration is highly symmetric. In some cases, this symmetry can be inherited by the numerical solution creating an unlikely physical realization of the flow field around the sphere. Two measures are implemented to prevent this problem from occurring. First, the grid is altered at the sphere's surface in block 10 on the $-x$ side of the sphere. A perturbation is made along an arc that extends across the block face; at the block boundary, the perturbation is zero while at the center of the arc, the perturbation is a maximum. The shape of the perturbation is that of an arc-shaped indentation on the sphere. A picture of this perturbation is shown in Figure 2.

Another important aspect of computing a flow solution for the sphere is that of boundary conditions. As one may expect, boundary conditions have to be established for this problem in each block. The lateral surfaces, those with constant index coordinates, ($i = 1$, IMAX or $k = 1$, KMAX) are communicating interfaces that exchange data with neighboring blocks. This type of condition is not a true boundary condition. The inner surface boundary is quite simple. A viscous (no-slip) boundary condition is enforced for the inner ($j = 1$) surface for each block. The outer boundary is a bit more complicated. The yz -plane separates the regions of inflow from the regions of outflow. Given the order in which block grids are computed, the outer ($j = JMAX$) boundary for blocks 1 through 12 is designated as an inflow. The JMAX boundary for the remaining blocks 13 through 24 is designated as a supersonic outflow. LESLIE3D allows the user to specify the type of inflow and outflow as either characteristic variable for subsonic flow or interpolated for supersonic flow. Although the boundary conditions are specified in an input file by the user, these conditions are read by the pre-processor (pre_les3d) and formally set in LESLIE3D's processor communication files.

LESLIE3D also requires that the user specify initial conditions. For the purposes of this work, initial conditions are specified in an initial restart file REST_000.DATA created in the data directory for each block. Pressure, temperature, velocity components, subgrid kinetic energy and initial chemical species mass fractions must be set by the user. For the problems solved here, uniform flow conditions are set for the entire flow field without regard for the presence of the

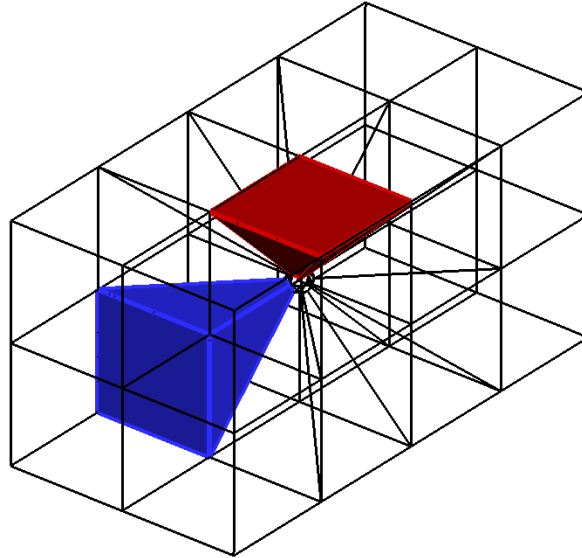


Figure 3. Grid block arrangement for the simulation of subsonic flow outside of the sphere

sphere's surface. Starting the numerical solution in this way creates a "slug flow" condition that is non-physical. Solver time is required for LESLIE3D to advect this non-physical slug of flow from the solution. For refined grids, this process can be time consuming. An approach used in this case is to first run the problem on a uniform (equally spaced) radial grid. This process allows larger time steps and can more quickly dispense with the slug flow. At this point, the numerical solution is remapped onto a refined grid, and LESLIE3D is restarted. The solution is, of course, incorrect near the body surface due to the lack of refinement, so LESLIE3D is run forward with the LES algorithms activated until the flow near the surface becomes stationary. Stationarity can be verified by examining time histories for flow variables say, vorticity magnitude and subgrid kinetic energy. A series of restart files taken after the flow solution has become stationary may be used to calculate the force time histories, e.g. the drag force in time.

The spherical grid presented above functions well for supersonic flow problems but not for subsonic flow. At subsonic speeds, the treatment of inflow and outflow boundaries requires special attention. At these boundaries, acoustic waves can enter or exit the computational domain. As a result, these waves can alter the numerical solution. A better grid is generated for this problem by projecting the outer surfaces of the component spherical blocks onto flat planes. Rectangular inflow and outflow blocks, numbered 25 through 32, are added to the grid to implement characteristic variable boundary conditions. This grid arrangement is shown in Figure 3. The blue block shown in Figure 3 connects the sphere to one of brick shaped inflow blocks. Similar blocks connect to the brick-shaped outflow blocks. The red block extends laterally to the outer boundary which is coded as a slip surface. LESLIE3D's characteristic variable inflow/outflow boundary conditions require grid blocks with a higher degree of uniformity and more importantly, coincident indicial axis directions. The revised grid design satisfies these requirements.

4.0 RESULTS

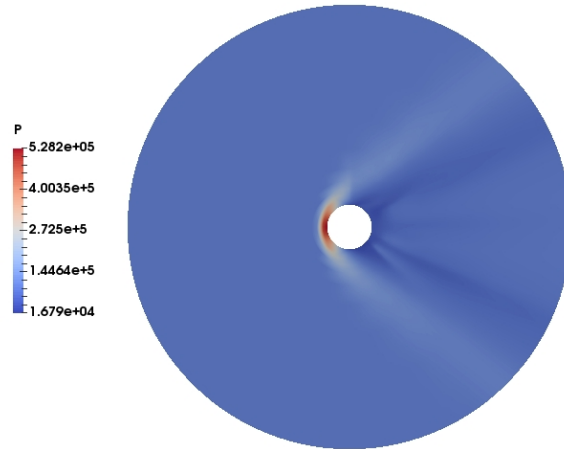


Figure 4. Slice pressure plot on the xy -plane of the sphere flow field at Mach 2, units in Pascals

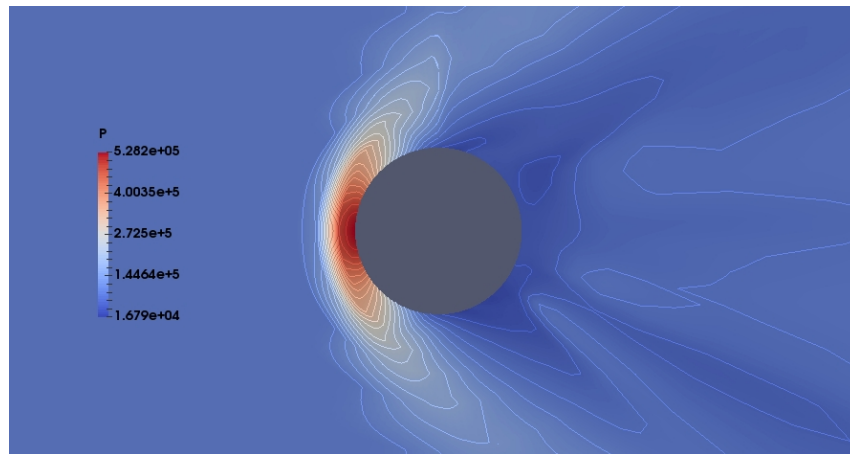


Figure 5. Contoured slice pressure plot on the xy -plane of the sphere flow field at Mach 2, units in Pascals

4.1 Supersonic Test Case - Flow Field Results

The first test case considered assumes that the sphere is traveling at Mach 2, altitude 1000 feet. The altitude data allows the freestream pressure and density to be set based upon atmospheric tables. The Reynolds number is computed as about 8.1 million based upon the sphere's diameter of 0.2 meters. At this altitude, the freestream velocity is 667.7 meters per second. Figure 4 contains a slice plot of the pressure field taken along the xy -plane. The curved shock wave is evident as is the wake region even though the grid is not zoned well in the far field. Rather the best zoning is adjacent to the body to support better drag calculations. Figure 5 contains a contoured slice plot of pressure taken from the flow field along the xy -plane at 12.5 ms solution time. In this case, the region near the sphere's surface is magnified for better viewing. The stagnation region is clearly visible, and the wake region is characterized by asymmetric contouring, just as expected. Temperature plots show similar behavior. A slice plot along the xy -plane is presented in Figure 6 with absolute temperature indicated in Kelvin. The high temperature stagnation region is evident, but more interestingly, the gas heated in the boundary layer washes off from the sphere's surface and advects into the wake. This phenomenon is also visible in Figure 7, a close in view of the same

slice.

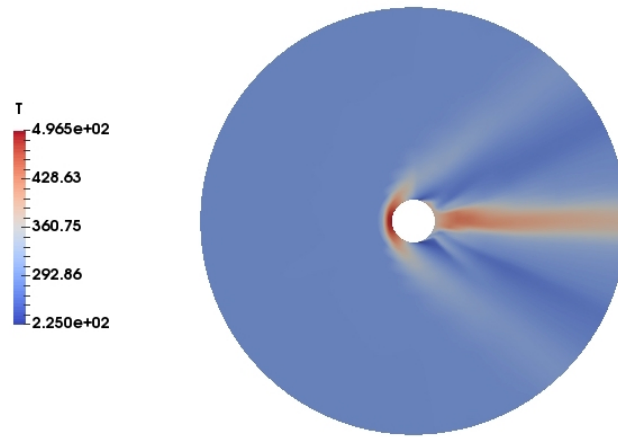


Figure 6. Full field slice temperature plot of the sphere flow field at Mach 2, units in Kelvin

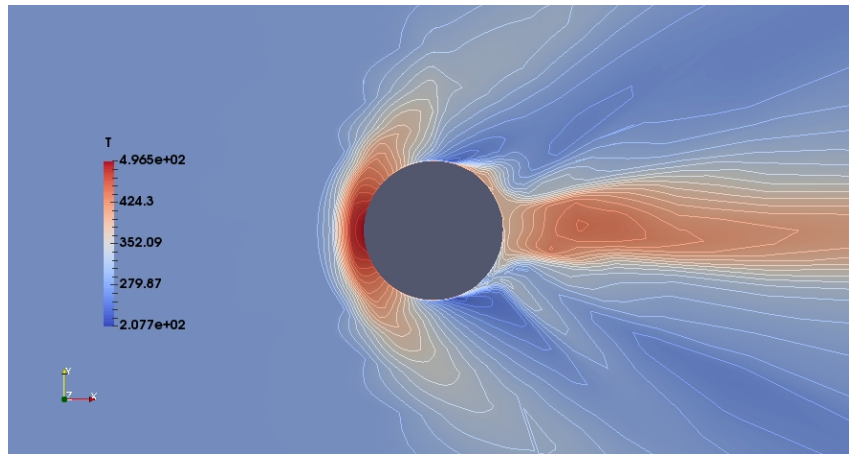


Figure 7. Contoured slice temperature plot of the sphere flow field at Mach 2, units in Kelvin

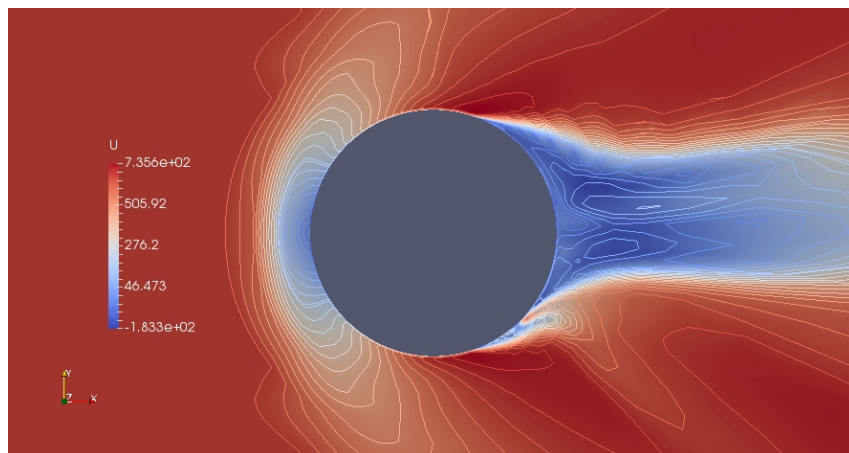


Figure 8. Slice plot of u velocity with contours of velocity magnitude at 13.61 ms; units are m/s

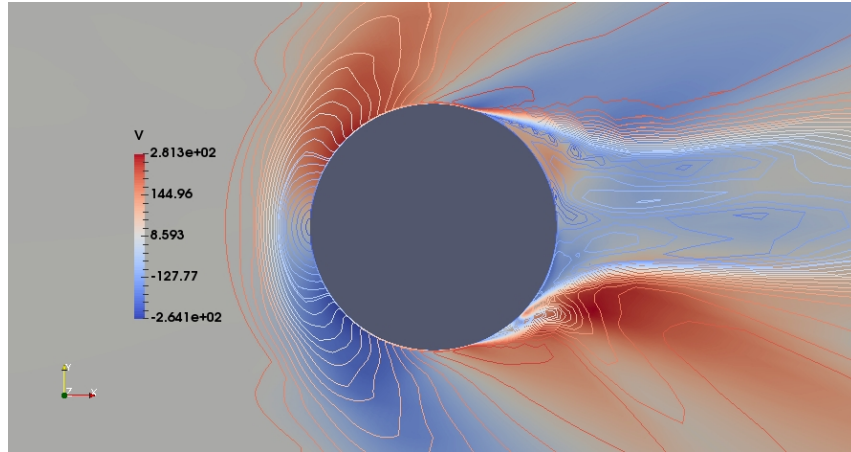


Figure 9. Slice plot of v velocity with contours of velocity magnitude at 13.61 ms; units are m/s

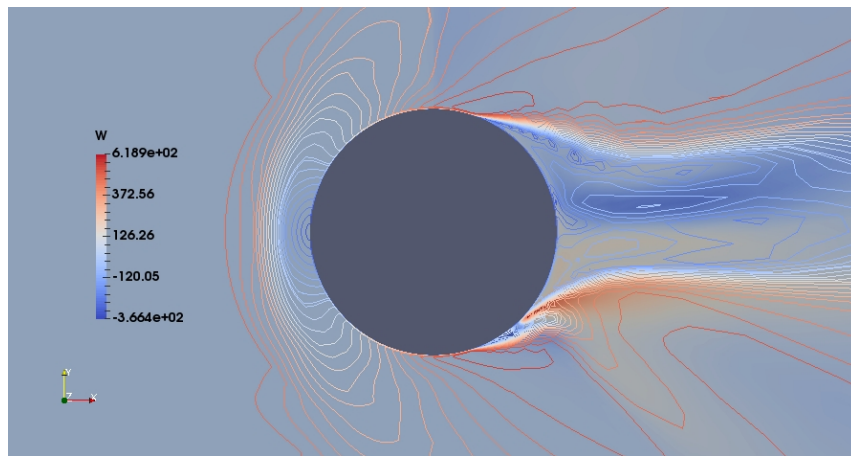


Figure 10. Slice plot of w velocity with contours of velocity magnitude at 13.61 ms; units are m/s

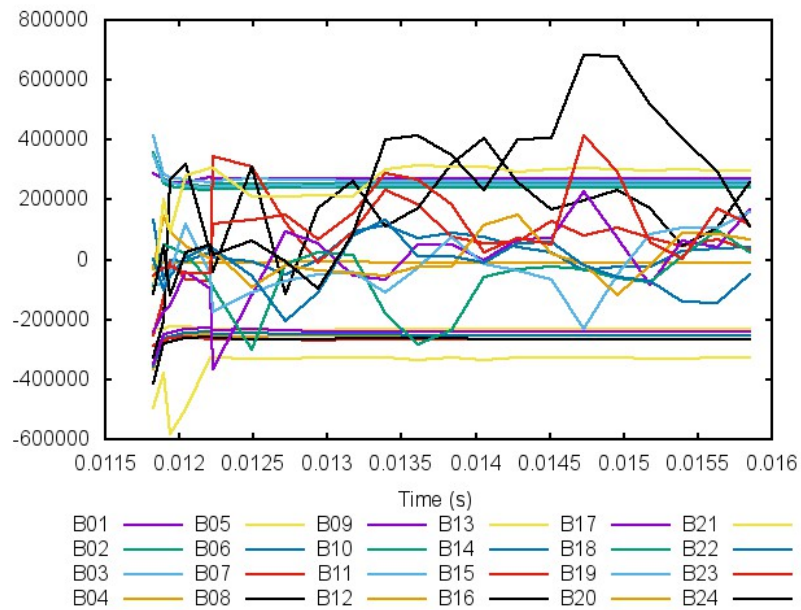


Figure 11. Time history plots for x-component of vorticity, units s^{-1}

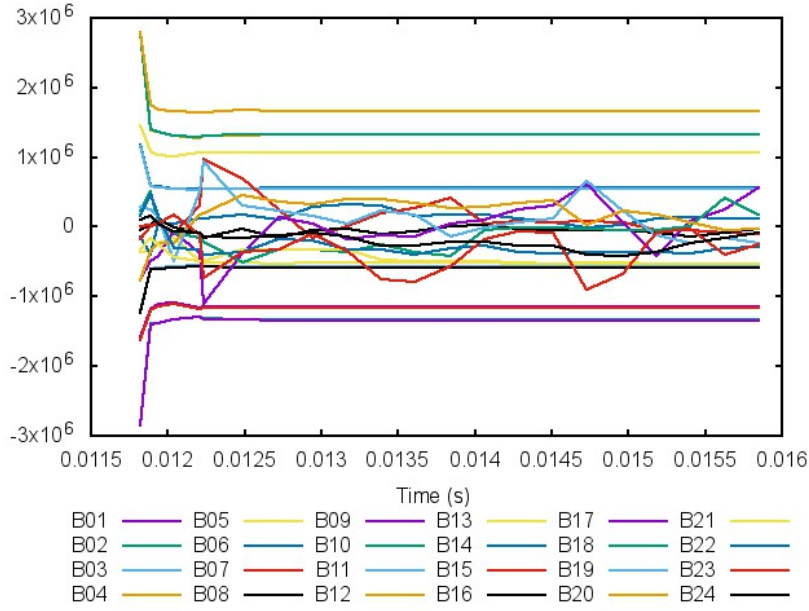


Figure 12. Time history plots for y-component of vorticity, units s^{-1}

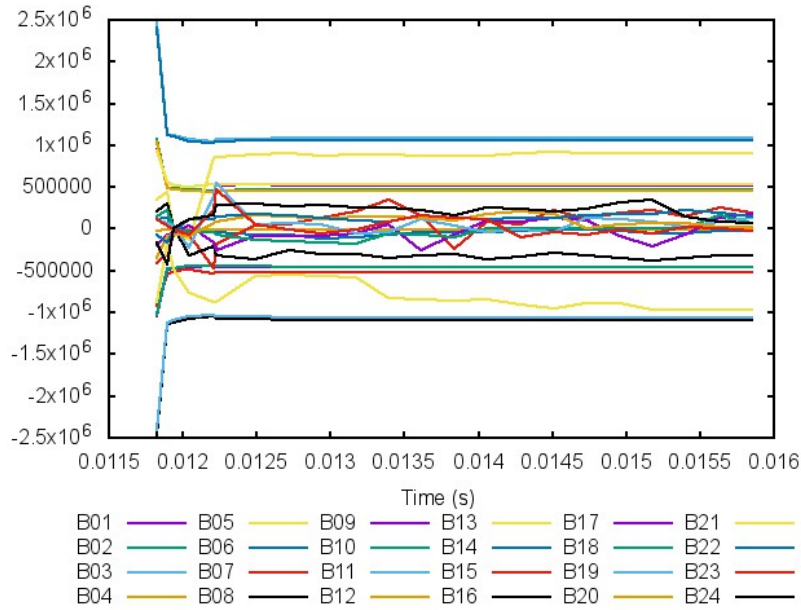


Figure 13. Time history plots for z-component of vorticity, units s^{-1}

Figure 8 is an interesting slice plot of u velocity, the component of flow in the stream (or x) direction. Contour lines of velocity magnitude are applied to the plot. Flow separation is evident since gas is observed propagating upstream in the region near the back of the sphere. A recirculation region is likely to exist in the wake. This idea is reinforced by Figure 9, a similarly designed plot of v velocity, the vertical component. In this case, we can see masses of fluid alternatively rising and falling in the wake indicative of a recirculating flow, at least intermittently. This idea is also borne out by Figure 10, a plot of w velocity, the component in the z direction. In this case, bright red color indicates flow out of the page while blue is in the opposite direction. From this evidence, it is obvious that this flow field is fully three-dimensional.

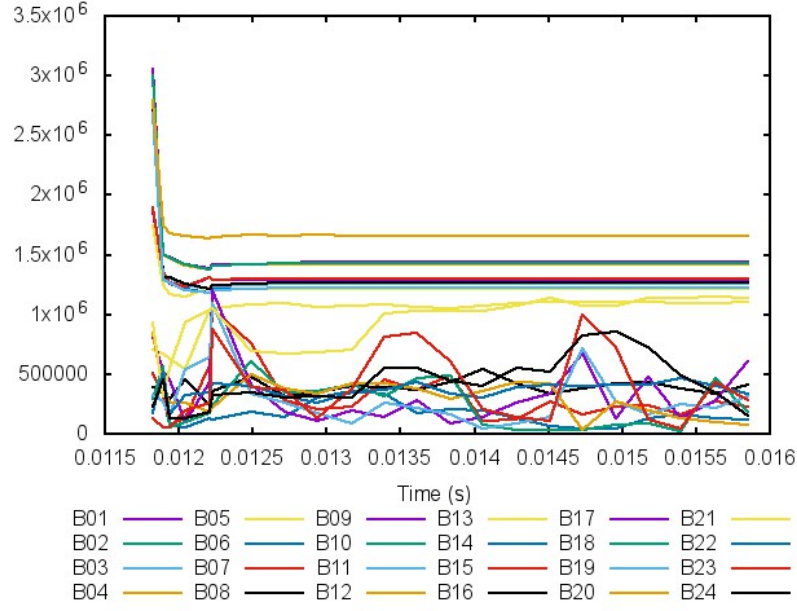


Figure 14. Time history plots for vorticity magnitude, units s^{-1}

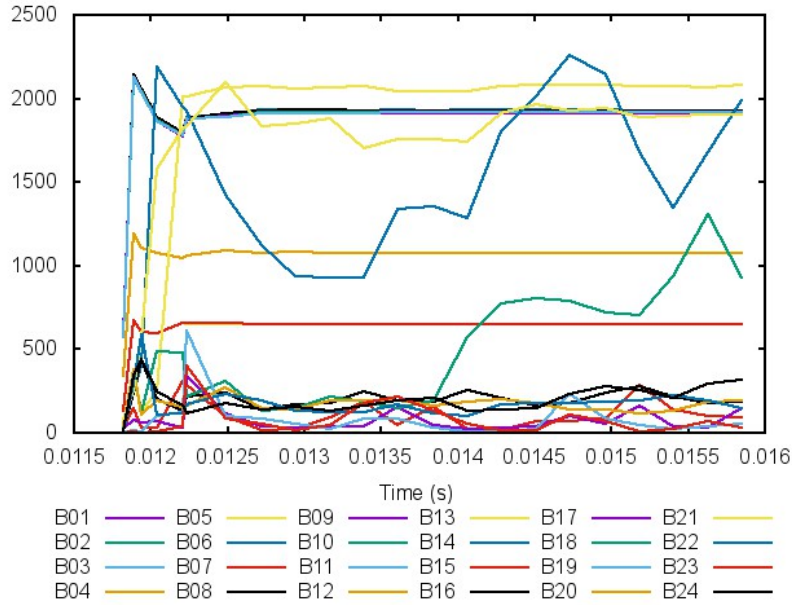


Figure 15. Time history plots for subgrid kinetic energy, units m^2/s^2

Prior to post-processing solver output data for drag information, it is necessary to show that the flow field is stationary. That is to say, its statistical quantities are unchanging. We can illustrate this idea by the use of time histories of fluctuating quantities like vorticity or subgrid kinetic energy. Also, we examine how these properties behave on the sphere's surface in time. If these properties exhibit periodic behavior in time, then the flow is stationary. To examine the approach to stationarity, we consider Ω_x , Ω_y , Ω_z and Ω , the x , y and z components of vorticity along with the vorticity magnitude. Also, the subgrid kinetic energy k^{sgs} is studied. These properties are selected because of their strong roles in the evolution of turbulence. Time histories are sampled on the sphere's surface with exactly one sampling point per block. In most cases, the

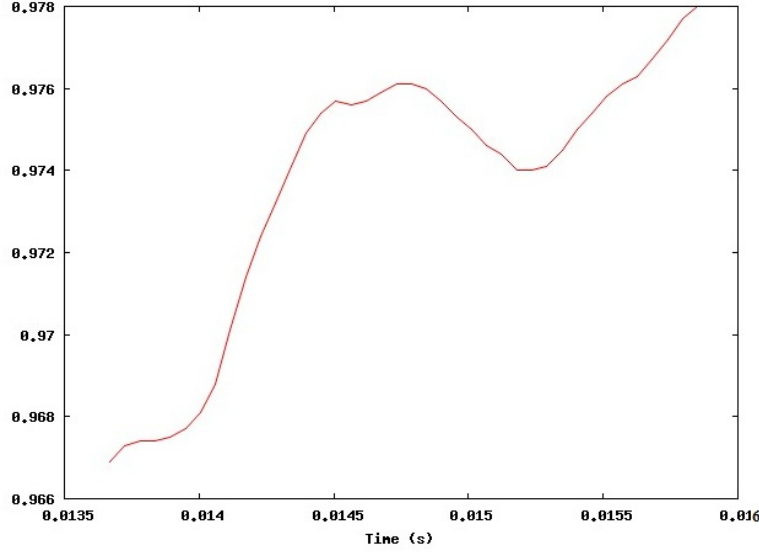


Figure 16. Drag coefficient time history for the sphere at Mach 2.0

sampling point is located at the center of the block's inner surface. The two exceptions are blocks 12 and 18, where the sample point is located near the block boundary. Time histories for Ω_x , Ω_y , Ω_z and Ω are shown in Figures 11, 12, 13 and 14, respectively. Time evolution of k^{sgs} is shown in Figure 15. In each of these figures, we observe that envelopes form around the time history traces for almost all of the sample points. The exceptions are the x -component of vorticity and with subgrid scale kinetic energy. Traces for Ω_x depart from the envelope for sample points 23 and 24. These points are located on the trailing section of the sphere in the $+y, +z$ octant. The excursion in k^{sgs} occurs at sample point 14 on the trailing section of the sphere in the $+x, -y, -z$ octant. Both of these regions are subject to vortex shedding and recirculation, so it is expected that both of these properties rise and fall in time. Histories formed at the remainder of the sample points exhibit nearly periodic behavior. Based upon these plots, the flow field is sufficiently stationary to admit force calculations. Force components (particularly drag, the force exerted in the $+x$ direction) are obtained by post-processing a series of solution files. For the supersonic solution, a time history for the drag coefficient is shown in Figure 16. The archived drag coefficient for this configuration is essentially 1.0, so the numerical solution agrees well with this datum.[22]

4.2 Subsonic Test Case - Flow Field Results

The previous test case examines the flow field around the sphere at high Reynolds number where the drag curve levels out. In itself, that test case is very important because high Reynolds number situations are widely applicable. Still, it is important to verify the performance of our computer codes at low Reynolds number where the drag curve exhibits changes. At a Reynolds number of approximately 400,000, the drag curve dips sharply due to boundary layer separation.[3] It is desirable to verify our computer codes for this case. The flow geometry and grids remain the same as in the preceding case. The freestream flow conditions do change. This problem is conducted at an altitude of 1,000 feet and Mach 0.1, a low speed flow condition corresponding to about 33.3 m/s. A major change in problem set-up involves LESLIE3D's boundary conditions. At

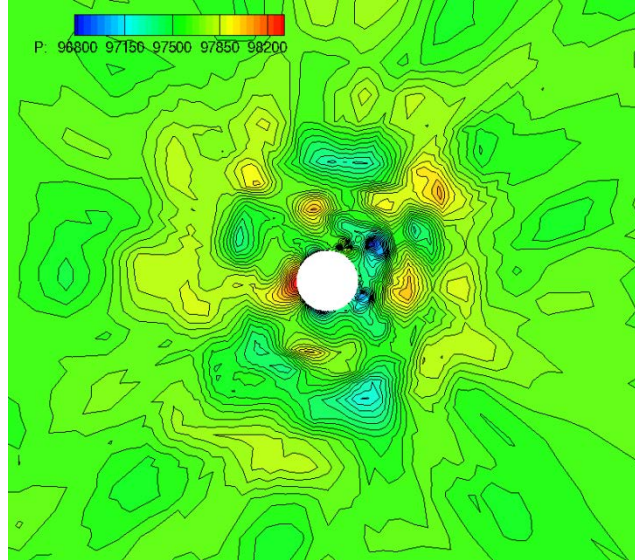


Figure 17. Slice plot of the pressure field for the subsonic solution at 43.68 ms

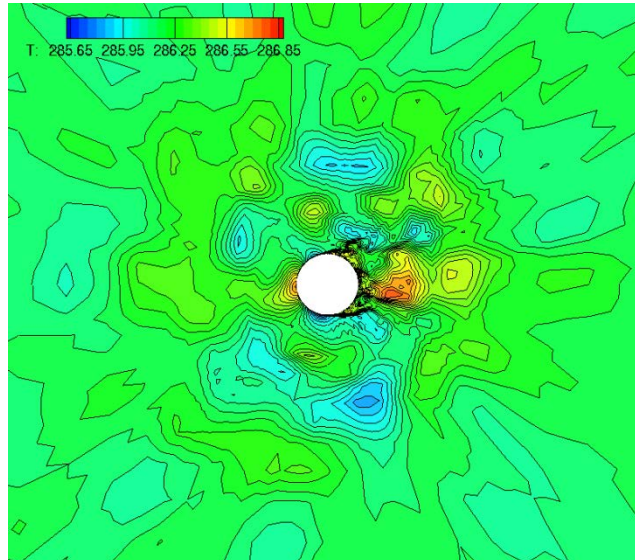


Figure 18. Slice plot of the temperature field for the subsonic solution at 43.68 ms

this flow speed, acoustic waves can travel in both directions, with and against the flow. Physically, this means that an acoustic signal can travel from the sphere to the numerical inflow boundary altering the flow at that location. This situation cannot happen in supersonic flow, so different algorithms must be used to account for this type of wave propagation. To properly capture physics at the inflow boundary, characteristic variable boundary conditions are employed.[21] This type of algorithm uses entropy, vorticity and acoustic wave information from the different flow directions to solve simultaneously for the inflow conditions. The outflow boundary is also structured in a similar manner. Characteristic boundary conditions are employed at the outflow to set properties at the outflow plane. Sample plots of the flow field are shown below at solution time 43.68 ms. Figure 17 contains a slice plot of pressure while Figure 18 contains a plot of temperature. MacCormack's space scheme is utilized for computing the subsonic solution since the flow field is turbulent but completely free of shock waves. Vortex shedding is evident in both Figures 17 and 18; the downstream direction is to the right in both figures. Note the high pressure stagnation point

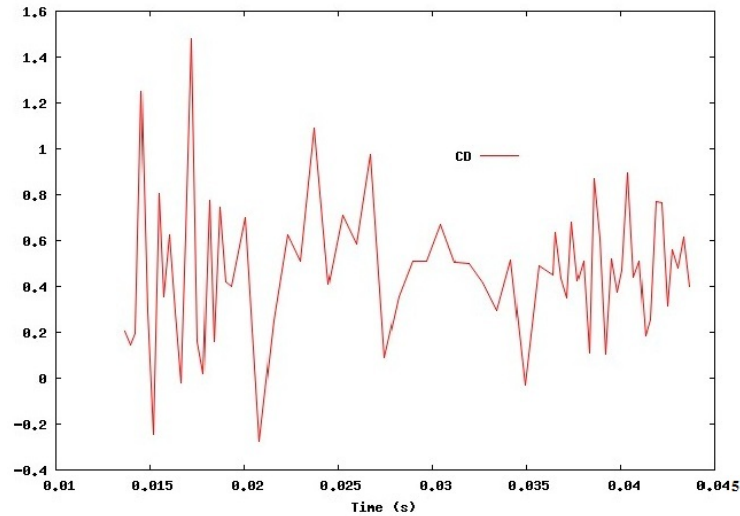


Figure 19. Drag coefficient time history for the sphere at Mach 0.1

existing on the windward side of the sphere in Figure 17. The elevated temperature generated in the boundary layer is shed into the flow field at the back of the sphere. A high temperature locus corresponding to this region is visible in Figure 18. Vortices shed somewhat irregularly from the sphere creating oscillatory forces, and the drag force may be extracted by post-processing. Accordingly, a time history for the drag coefficient is shown in Figure 19. The drag coefficient is unsteady, but its average is calculated as 0.464. Note that the early time values (less than 0.02 s) are taken before the solution has become stationary. The average C_D for this Reynolds number agrees quite well with the archived coefficient plot recorded in Schlichting.[3]

5.0 CONCLUSIONS

This report focuses on a validation study conducted for the Large Eddy Simulation with Linear Eddy modeling in 3 Dimensions (LESLIE3D) multiphase physics computer program. This computer program has application for air-to-air missile aerodynamics, so it is important to demonstrate user capabilities for LESLIE3D and also to ensure that solution data can be accurately post-processed to extract aerodynamics data. Aerodynamic drag is of principal interest in this report. The validation problem selected for analysis is the turbulent, multi-species flow around a sphere, a typical bluff body often used for validation. The flow field is computed first at Mach 2.0, Reynolds number 8 million and then at Mach 0.1, Reynolds number 400,000. The first problem involves a shocked flow field while the latter flow field is smooth. Both flow fields are turbulent and set at an altitude of 1,000 feet. In each case, a significant amount of work is invested in the generation of grids for these two flow fields. In each case, the appropriate numerical boundary conditions are applied for the two different flight conditions. Drag coefficients are computed from the numerical solution for these problems. For the supersonic problem, the average drag coefficient is computed as 0.973, and for the subsonic case, the average drag coefficient is calculated as 0.464. These results compare favorably with archived data. Accordingly, these results serve to validate the methodology for problem set-up employed in this work. Our post-processing algorithms are validated simultaneously. Validation problems recommended for future accomplishment may involve the oblate spheroids or hemisphere-cylinder configurations. These problems may be solved for hypersonic flight conditions with atmospheric chemical reactions.

REFERENCES

1. Sankaran, V. and Menon, S., LES of spray combustion in swirling flows, *Journal of Turbulence*, Vol. 3, No. 1, 2002, pp. 011.
2. Nance, D.V., Stochastic Estimation via Polynomial Chaos, Technical Report, AFRL-RW-EG-TR-2015-108, 2015.
3. Schlichting, H., *Boundary-Layer Theory*. McGraw-Hill, Inc., New York, New York, 1979.
4. Anderson, J.D., Jr., *Hypersonic and High Temperature Gas Dynamics*, McGraw-Hill, Inc, New York, New York, 1989.
5. Genin, F. *Study of Compressible Turbulent Flows in Supersonic Environment by Large-Eddy Simulation*. Doctoral Dissertation, Georgia Institute of Technology, 2009.
6. Narasimhan, M.N.L., *Principles of Continuum Mechanics*. John Wiley & Sons, Inc., New York, New York, 1993.
7. Tennekes, H. and Lumley, J.L., *A First Course in Turbulence*. The MIT Press, Cambridge, Massachusetts, 1992.
8. Lesieur, M., *Turbulence in Fluids*, 2nd Revised Ed., Fluid Mechanics and Its Applications, Vol. 1, Kluwer Academic Publishers, Boston, Massachusetts, 1990.
9. Menon, S., Yeung, P.-K. and Kim, W.-W., "Effect of subgrid models on the computed interscale energy transfer in isotropic turbulence", *Computers & Fluids*, Vol. 25, No. 2, 1996, pp. 165-180.
10. Sankaran, V., *Sub-grid Combustion Modeling for Compressible Two-Phase Reacting Flows*. Doctoral Dissertation, Georgia Institute of Technology, 2003.
11. Hirsch, C., *Numerical Computation of Internal and External Flows, Vol. 2, Computational Methods for Inviscid and Viscous Flows*. John Wiley & Sons, New York, NY, 1990.
12. Burden, R.L., Faires, J.D. and Reynolds, A.C., *Numerical Analysis*, 2nd Ed., Prindle, Weber & Schmidt, Boston, Massachusetts, 1981.
13. Toro, E.F., *Riemann Solvers and Numerical Methods for Fluid Dynamics - A Practical Introduction*. Addison-Wesley Publishing Co., Inc., Boston, Massachusetts, 1999.
14. Sod, G.A., *Numerical Methods in Fluid Dynamics: Initial and Boundary Value Problems*. Cambridge University Press, New York, New York, 1985.
15. Roe, P.L., "Approximate Riemann Solver, parameters vector and difference schemes", *Journal of Computational Physics*, Vol. 43, 1981, pp. 357-371.

16. Glaister, P., "An approximate linearised Riemann solver for the Euler equations for real gases", *Journal of Computational Physics*, Vol. 74, 1988, pp. 382-408.
17. Harten, A., Lax, P.D. and van Leer, B., "On upstream differencing and Godunov-type schemes for hyperbolic conservation laws", *SIAM Review*, Vol. 25, pp. 35-61, 1983.
18. Einfeldt, B., "On Godunov-type methods for gas dynamics", *SIAM Journal of Numerical Analysis*. Vol. 25, No. 2, pp. 294-318, 1988.
19. Toro, E.F., "Restoration of the contact surface in the HLL Riemann solver", *Shock Waves*. Vol. 4, pp. 25-34, 1994.
20. Collela, P. and Woodward, P., "The piece-wise parabolic method for hydrodynamics", *Journal of Computational Physics*. Vol. 54, pp. 174-201, 1984.
21. Poinso, T.J. and Lele, S.K., "Boundary conditions for direct simulations of compressible viscous flows", *Journal of Computational Physics*. Vol. 1, No. 1, 1992, pp. 104-129.
22. Spearman, M.L. and Braswell, D.O., Aerodynamics of a Sphere and an Oblate Spheroid for Mach Numbers from 0.6 to 10.5 Including Some Effects of Test Conditions, NASA Technical Memorandum 109016, 1993.

LIST OF ACRONYMS, ABBREVIATIONS, AND SYMBOLS

This section contains brief definitions of various terms and acronyms used throughout this document. Only terms and acronyms whose definitions are considered uncommon are included.

HLLC	Harten, Lax and van Leer Contact preserving
LDKM.....	Locally Dynamic subgrid Kinetic Energy Model
LES	Large Eddy Simulation
LESLIE3D	Large Eddy Simulation with Linear Eddy modeling in 3 Dimensions
MUSCL.....	Monotone Upstream centered Schemes for Conservation Laws

C_D	Drag coefficient
C_P	Constant specific heat at constant pressure
C_v	Constant volume specific heat capacity
D_k	Species diffusion coefficient
E	Energy per unit volume
e	Internal energy per unit mass
h	Sensible enthalpy
MW_n	Molecular weight of species n
P	Pressure
q_i	Heat flux vector component
R	Species gas constant
R_{univ}	Universal gas constant
Re	Reynolds number
sgs	Subgrid scale
T	Temperature
u_i	Cartesian velocity component
V	Velocity magnitude
\vec{V}	Velocity vector
V_{ik}	Diffusion velocity
Y_k	Species mass fraction

x_i	Cartesian space coordinate
λ	Bulk viscosity
κ	Heat transfer coefficient
δ	Delta function
ρ	Density
τ_{ij}	Shear stress tensor
μ	Dynamic viscosity
$\dot{\omega}_k$	Species production rate

DISTRIBUTION LIST
AFRL-RW-EG-TR-2016-092

*Defense Technical Info Center
8725 John J. Kingman Rd Ste 0944
Fort Belvoir VA 22060-6218

AFRL/RWML (1)
AFRL/RWORR (STINFO Office) (1)